The Astrophysical Journal, 988:126 (11pp), 2025 July 20 https://doi.org/10.3847/1538-4357/ade23b

Varstrometry for Off-nucleus and Dual Sub-Kpc AGN (VODKA): Long-slit Optical Spectroscopic Follow-up with Gemini/GMOS and Hubble Space Telescope/STIS

Yu-Ching Chen[1,2], Arran C. Gross[2], Xin Liu[2,3], Yue Shen[2,3], Nadia L. Zakamska[1], Hsiang-Chih Hwang[4], and Ming-Yang Zhuang[2]
[1] Department of Physics and Astronomy, Johns Hopkins University, Baltimore, MD 21218, USA; ycchen@jhu.edu
[2] Department of Astronomy, University of Illinois at Urbana-Champaign, Urbana, IL 61801, USA; xinliuxl@illinois.edu
[3] National Center for Supercomputing Applications, University of Illinois at Urbana-Champaign, Urbana, IL 61801, USA
[4] School of Natural Sciences, Institute for Advanced Study, Princeton, 1 Einstein Drive, NJ 08540, USA
Received 2024 September 13; revised 2025 May 17; accepted 2025 June 4; published 2025 July 18

Abstract

High spatial and spectral resolution observations are essential for identifying subarcsecond dual and lensed quasars and confirming their redshifts. We present Gemini/Gemini Multi-Object Spectrograph and Hubble Space Telescope/STIS optical spectra for 27 dual quasar candidates selected based on their variability-induced astrometric noise or double detections in Gaia (the Varstrometry for Off-nucleus and Dual sub-Kpc AGN (VODKA) project). From this follow-up, we spectroscopically identify 11 star superpositions and seven dual/lensed quasars. Among the remaining targets, two are likely dual/lensed quasars based on additional radio imaging, while the rest are quasars with unknown companions. Without prior photometric or spectroscopic selection, we find the star contamination rate to be 41%–67%, while the dual/lensed quasar fraction is $\gtrsim$26% in the follow-up VODKA sample. However, when combined with existing unresolved spectra and spatially resolved two-band color cuts, the dual/lensed quasar fraction can be increased to $\gtrsim$67%. Our study highlights the need for high-quality spectral data, including a signal-to-noise ratio of at least 20, spatial resolution that is at least twice finer than the source separation, and a spectral resolution of $R \gtrsim 1000$, in order to separate close sources, exclude stellar superpositions, and reliably identify dual quasars.

Unified Astronomy Thesaurus concepts: Spectroscopy (1558); Strong gravitational lensing (1643); Double quasars (406); Active galactic nuclei (16); Supermassive black holes (1663); Quasars (1319)

1. Introduction

Most nearby massive galaxies harbor a supermassive black hole (SMBH) at their centers (J. Magorrian et al. 1998; J. Kormendy & L. C. Ho 2013). Cold dark matter models often depict hierarchical structure formation and galaxy mergers (S. D. M. White & C. S. Frenk 1991; J. F. Navarro et al. 1996; S. Cole et al. 2000). When two galaxies merge, gas can accrete onto the central SMBHs as tidal forces generate non-axisymmetric structures in the companion galaxy, which torque the gas and drive it toward the nuclei (L. Hernquist 1989; J. E. Barnes & L. Hernquist 1996; J. C. Mihos & L. Hernquist 1996; P. F. Hopkins & E. Quataert 2010). In addition to these tidal torque-induced inflows, ram-pressure sweeping at pericentric passage can effectively decouple gas from stars, reducing the gas's angular momentum and further enhancing central inflows (J. E. Barnes 2002; P. R. Capelo & M. Dotti 2017). If both SMBHs are active and still within their host galaxies' potential, they are known as dual quasars. While cosmological simulations show increased quasar activity and dual quasar fraction in the late-stage mergers (L. K. Steinborn et al. 2016; A. De Rosa et al. 2019; Y. M. Rosas-Guevara et al. 2019; M. Volonteri et al. 2022; N. Chen et al. 2023a), the observational evidence for the link between quasar activity and mergers is still debated (L. Fan et al. 2016; M. Mechtley et al. 2016; S. L. Ellison et al. 2019; P. Breiding et al. 2024). The dual quasar phase is an excellent stage to study quasar triggering and its connection to galaxy mergers (M. Volonteri et al. 2022).

Identifying dual quasars is challenging due to their rarity and close separations, particularly at higher redshifts ($z > 1$) when the angular diameter distance is large (1 8 kpc at z 2). In recent years, large sky surveys with high angular resolution, such as Gaia, have become valuable tools for finding dual and lensed quasars (C. A. Lemon et al. 2018, 2019; Y.-C. Chen et al. 2022; C. Lemon et al. 2023). Despite the introduction of various techniques to discover small-separation ($\lesssim$1) dual quasar candidates (H.-C. Hwang et al. 2020; F. Mannucci et al. 2022), only a small fraction of these candidates have been confirmed (Y.-C. Chen et al. 2023b; A. Ciurlo et al. 2023; F. Mannucci et al. 2023; M. Scialpi et al. 2024). One notable effort in finding close-separation dual quasars is the Varstrometry for Off-nucleus and Dual sub-Kpc AGN (VODKA) project (Y. Shen et al. 2019; H.-C. Hwang et al. 2020). The VODKA project aims to discover unresolved dual quasars by analyzing centroid jitters from the non-coherent quasar light from two sources. With dozens of dual quasar candidates discovered by the VODKA project, spectroscopic follow-ups are essential to confirm their nature (Y.-C. Chen et al. 2022).

In this paper, we present optical spectroscopic observations for 27 targets from the VODKA project. We provide classifications based on spectra from the Hubble Space Telescope (HST) and the Gemini Observatory, along with other auxiliary data. The paper is organized as follows. Section 2 describes the data reduction and analysis procedures, as well as the spectral fitting details. In Section 3, we show the HST and Gemini spectra for the 27 targets and provide our

best classifications. Section 4 presents the sample category breakdown, highlights the cautionary case of J1649+0812 with an apparent velocity offset, and discusses implications for future spectroscopic studies. We summarize our findings in Section 5. We adopt a flat ΛCDM cosmology with $\Omega_\Lambda = 0.7$, $\Omega_m = 0.3$, and $H_0 = 70\,\mathrm{km\,s^{-1}\,Mpc^{-1}}$ throughout this paper.

2. Observations, Data Reduction, and Analysis

2.1. Target Selection: Dual Quasar Candidates

The 27 targets in this paper are the dual/lensed quasar candidates with small separations (<1) discovered using Gaia astrometry and HST images (Y.-C. Chen et al. 2022). The sample consists of 14 Gaia-resolved targets with separations $\gtrsim$0.″5 and 13 Gaia-unresolved targets selected by the astrometric technique, varstrometry. The varstrometry technique utilizes quasars' strong variability and the non-synchronized emission of two nuclei to discover unresolved dual quasars (Y. Shen et al. 2019; H.-C. Hwang et al. 2020). To confirm the nature of these candidates, we conducted a series of spectroscopic follow-up observations using HST and the Gemini Observatory. In addition to the spectroscopic campaign, we carried out imaging programs with the Very Large Array in radio and HST in the near-infrared to detect lens galaxies, study tidal features, and investigate radio properties. These findings are reported in a companion paper (A. C. Gross et al. 2024, in preparation).

2.2. HST/STIS

Out of 27 targets, 22 were observed with HST using the Space Telescope Imaging Spectrograph (STIS) during cycles 28 and 29 in 2021-2022 under programs GO-16210 and GO-16887 (PI: X. Liu). All the HST data used in this paper can be found on MAST: doi:10.17909/a3ac-ny86. The observations utilized the G750L grating with a 52 × 0.″2 aperture, covering observed wavelengths from 5240 to 10270 Å, with a resolving power of R 500. The slit direction was rotated to capture both nuclei, guided by the HST-resolved images (Y.-C. Chen et al. 2022). Exposure times and additional observational details can be found in Table 1.

The STIS spectra were reduced using the `stis_cti` package, which corrects for trails and artifacts caused by charge transfer inefficiency effects (J. Anderson & L. R. Bedin 2010). Following the standard STIS calibration pipeline, `calstis`, we applied flat-field correction, bad-pixel removal, and cosmic ray rejection. The final one-dimensional (1D) spectra for each nucleus were extracted using a boxcar aperture of 7 pixels (0.″35). Figures 1 and 2 present the calibrated 1D spectra of all the targets observed with HST/STIS.

2.3. Gemini/Gemini Multi-Object Spectrographs

Sixteen targets were observed using the GMOS on both the Gemini-North and Gemini-South telescopes in 2021 and 2022, under several programs (GN-2020A-DD-106, GS-2020A-DD-106, GN-2022A-Q-139, GS-2022A-Q-148; PI: X. Liu, and GN-2020A-Q-232; PI: Y.-C. Chen). The observations used the R150 grating centered around 700 nm with slit widths ranging from 0.″5 to 0.″75, covering the observed wavelength range of 4000–10040 Å, with a resolving power R of 420–630. The typical seeing conditions were $\lesssim$0.″75 (within the 70th percentile in optical), and for targets with smaller separations (<0.″5), seeing was $\lesssim$0.″4 (within the 20th percentile in optical). Although photometric cloud conditions were not required, most targets were observed under photometric conditions, with no significant signal loss due to clouds. As with the HST/STIS spectra, the slit direction was rotated to capture both nuclei. Standard stars EG131, LTT1788, Wolf1346, and LTT4816 were observed with a similar setup for flux calibration. The exposure times and additional observational details are provided in Table 1.

We reduced the raw exposures using the Python wrapper of the `iraf` software. We perform bias subtraction and flat-field correction. Wavelength calibration was completed using arc exposures taken with the same configuration, and flux calibration was based on standard star exposures with the same grating. We dithered the exposures along both the spatial and spectral directions. The final 2D exposures were combined to eliminate artifacts, remove bad pixels, and fill detector gaps.

The typical seeing conditions for the Gemini observations ranged from 0.″5 to 0.″8, comparable to the nuclear separations of our targets. Since many of the targets were only marginally resolved, we opted for a two-component Gaussian fit rather than boxcar extraction. At each spectral element, we fit two-Gaussian components with fixed separations along the spatial direction, allowing the centroids and FWHMs to vary initially to account for distortions and seeing variations across the spectral direction. The centroids and FWHMs were then refitted with a cubic spline function. Final flux densities were derived by fitting two-Gaussian components with fixed separations and wavelength-dependent centroids and FWHMs, as determined by the cubic spline fit. Figure 3 presents the calibrated 1D spectra of all the targets observed with Gemini/GMOS.

3. Results

3.1. Spatially Resolved Spectra

We present the optical spectra of the 27 targets obtained from Gemini/GMOS and HST/STIS in this section. Figures 1 and 2 show the HST/STIS spectra of 22 targets. All targets are spatially resolved in the HST/STIS spectra, benefiting from HST's high angular resolution (0.″075 at 800 nm). For 80% of the targets, we identify the quasars' broad emission lines in at least one of the sources. However, given the faintness of our targets ($f_\lambda \lesssim 10^{-16}\,\mathrm{erg\,s^{-1}\,cm^{-2}\,\AA^{-1}}$), the typical signal-to-noise ratios are $\lesssim$ 10, making it challenging to identify stellar absorption lines.

Figure 3 shows the Gemini/GMOS spectra of 16 targets. Using the two-Gaussian component fitting method described in Section 2.3, we successfully decompose the two sources for most of our targets. We also examine the 1D spatial profiles of the wavelength-averaged spectra to ensure that the two nuclei are well modeled by Gaussian components and that their flux ratios are consistent with those observed in HST optical images. Some targets, including J1649+0812 and J1732-1335, are affected by contamination from the adjacent bright nucleus, which we discuss in the individual classifications in Section 3.2. Thanks to the higher signal-to-noise ratios compared to the STIS spectra, we can identify not only the broad emission lines from quasars but also the narrow emission lines and absorption lines from star interlopers. For the targets observed in program GS-2022A-Q-148, the spectra are truncated at 7700Å due to poor response in one of the CCDs.

Table 1
Observation Details for the 27 Targets from Gemini and HST

Abbreviated Name (J2000) (1)	Obs. Date (UT) (2)	Exp. Time (min) (3)	SNR (4)	R (5)	Telescope/Instrument (6)	Grating (7)	Program ID (8)
WISE J0241+7801	2022-05-11	40	5, 1	500	HST/STIS	G750L	HST-GO-16210
WISE J0246+6922	2021-12-28	39	9, 6	⋯	⋯	⋯	⋯
WISE J0536+5038	2021-12-12	30	12, 5	⋯	⋯	⋯	⋯
SDSS J0748+3146	2022-01-03	33	2, 2	⋯	⋯	⋯	⋯
SDSS J0749+2255	2021-02-16	36	5, 2	⋯	⋯	⋯	⋯
SDSS J0753+4247	2022-01-17	31	6, 2	⋯	⋯	⋯	⋯
SDSS J0823+2418	2022-01-13	30	7, 5	⋯	⋯	⋯	⋯
SDSS J0841+4825	2021-02-10	32	3, 3	⋯	⋯	⋯	⋯
SDSS J0904+3332	2021-02-28	36	5, 4	⋯	⋯	⋯	⋯
WISE J1613−2644	2021-02-27	36	2, 1	⋯	⋯	⋯	⋯
WISE J1755+4229	2022-04-01	35	12, 2	⋯	⋯	⋯	⋯
WISE J1852+4833	2021-05-13	36	6, 2	⋯	⋯	⋯	⋯
WISE J2048+6258	2021-02-15	39	4, 2	⋯	⋯	⋯	⋯
SDSS J2122−0026	2021-08-03	30	4, 3	⋯	⋯	⋯	⋯
WISE J0348−4015	2022-07-09	35	2, 1	500	HST/STIS	G750L	HST-GO-16887
SDSS J1327+1036	2022-05-28	31	2, 1	⋯	⋯	⋯	⋯
SDSS J1648+4155	2022-03-28	35	8, 2	⋯	⋯	⋯	⋯
WISE J1649+0812	2022-04-20	33	7, 3	⋯	⋯	⋯	⋯
WISE J1711−1611	2022-06-12	32	3, 2	⋯	⋯	⋯	⋯
WISE J1937−1821	2022-06-11	34	2, 2	⋯	⋯	⋯	⋯
WISE J2050−2947	2022-07-20	31	6, 3	⋯	⋯	⋯	⋯
WISE J2218−3322	2022-09-05	34	1, 0.3	⋯	⋯	⋯	⋯
SDSS J0841+4825	2020-05-21	31	71, 51	420	Gemini/GMOS	R150	GN-2020A-DD-106
SDSS J0904+3332	2020-05-21	31	54, 15	⋯	⋯	⋯	⋯
WISE J1314−4912	2020-02-23	31	43, 33	420	Gemini/GMOS	R150	GS-2020A-DD-106
WISE J1732−1335	2020-08-13	40	42, 34	420	Gemini/GMOS	R150	GN-2020A-Q-232
WISE J1804+3230	2020-08-14	40	38, 35	⋯	⋯	⋯	⋯
WISE J1852+4833	2020-07-02	60	52, 22	⋯	⋯	⋯	⋯
WISE J1857+7048	2020-07-29	60	40, 15	⋯	⋯	⋯	⋯
SDSS J0749+2255	2022-04-20	31	29, 19	630	Gemini/GMOS	R150	GN-2022A-Q-139
SDSS J0823+2418	2022-04-20	17	40, 36	420	⋯	⋯	⋯
SDSS J1225+4831	2022-04-20	23	31, 24	420	⋯	⋯	⋯
SDSS J1648+4155	2022-04-21	53	49, 14	630	⋯	⋯	⋯
WISE J1649+0812	2022-04-21	23	42, 37	630	⋯	⋯	⋯
WISE J1711−1611	2022-04-01	23	23, 18	420	Gemini/GMOS	R150	GS-2022A-Q-148
WISE J1937−1821	2022-06-11	26	21, 18	420	⋯	⋯	⋯
WISE J2050−2947	2022-06-12	20	33, 21	420	⋯	⋯	⋯
WISE J2218−3322	2022-11-17	40	16, 10	630	⋯	⋯	⋯

Note. Column (1): Target name. Column (2): Observation date. Column (3): Exposure time. Column (4): Median signal-to-noise ratio per spectral element for each source. Column (5): Spectral resolution $R = \lambda/\Delta\lambda$. Column (6): Telescope and instrument. Column (7): Grating name. Column (8): Program ID. The entries marked with "⋯" in (5), (6), (7), and (8) are the same as the first row in each block.

3.2. Classifications

Using the spectra from Gemini and HST, we perform the following steps to classify each target:

1. Identify quasars based on their broad emission lines and measure their redshifts.
2. Identify stars by detecting absorption lines, such as NaD, if present.
3. For featureless spectra without detected emission or absorption lines, identify quasars using deep radio imaging from A. C. Gross et al. (2024, in preparation).

Based on the spectra and auxiliary multiwavelength images, we identify seven dual/lensed quasars, 10 quasar-star superpositions, and one binary star. For the remaining nine targets, two are likely dual/lensed quasars. We are unable to conclusively determine the nature of the other seven targets but provide our best estimates based on the images and spectra. The classifications are listed in Table 2. Each group of targets is discussed in the following subsections.

3.2.1. Binary Stars and Quasar-star Superpositions

We detect at least one stellar absorption line (e.g., Na I, H , Ca II) from nearby foreground stars in the following 11 targets:

1. *J0246+6922*. A binary M-type star. Both sources exhibit broad, strong Ca II and TiO absorption lines, and extremely red colors in the HST spectra.

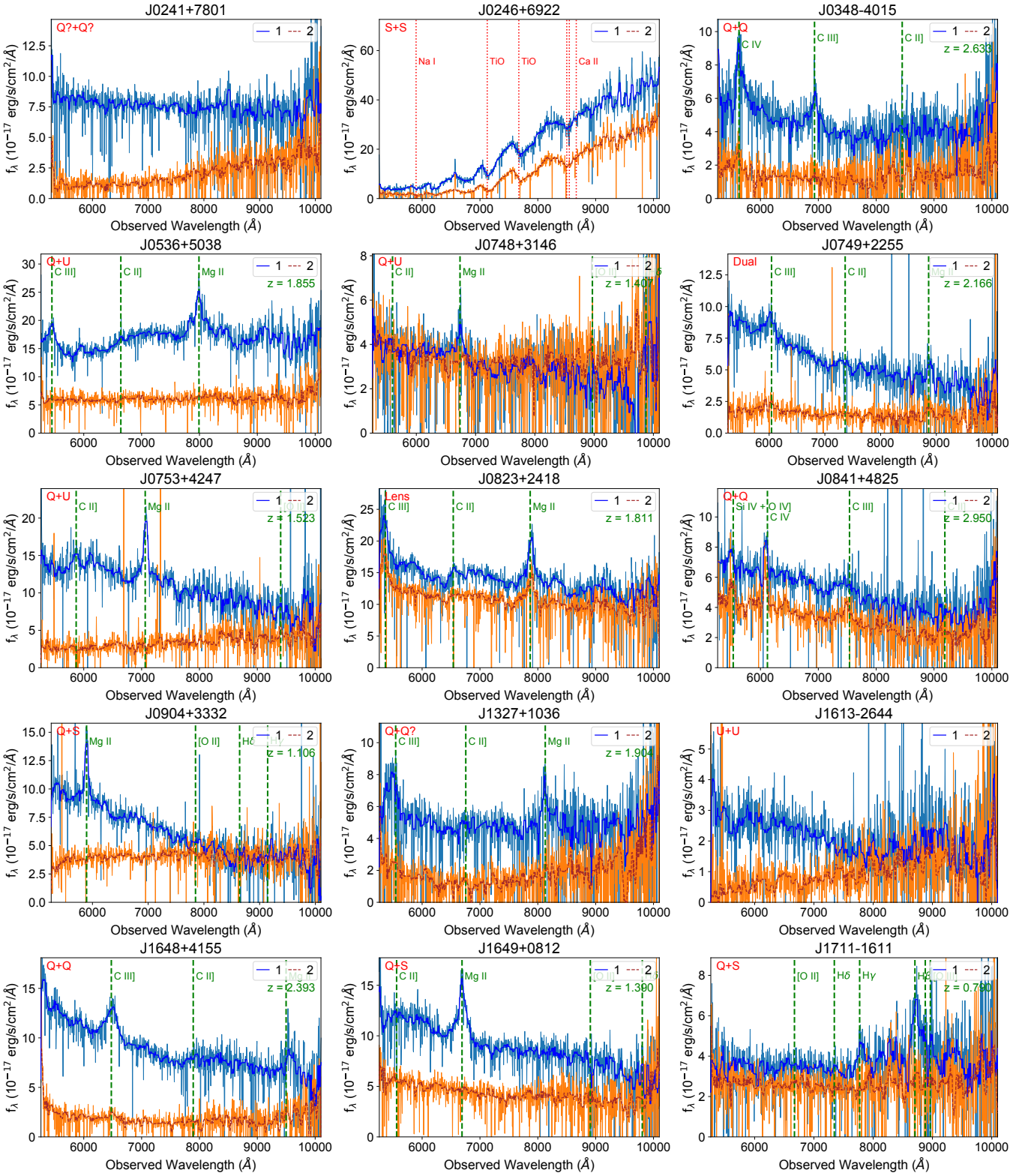

Figure 1. HST STIS optical spectra of 22 targets (15 in this figure and seven in Figure 2). Spatially resolved spectra for both sources are shown in solid blue and dashed orange lines. Green vertical dashed lines indicate the quasar's emission lines at the systemic redshift, displayed in the top-right corner. Red vertical dotted lines indicate stellar absorption features for star-superposition. Final classifications based on both Gemini and/or HST spectra are shown in the top-left corner. (Q: quasar, S: star, U: unknown, Dual: dual quasar, Lens: lensed quasar, ?: likely).

2. *J0904+3332*. $z = 1.106$ quasar + star. Source 1 shows broad Mg II emission lines at $z = 1.106$ in both HST and Gemini spectra. Source 2 shows Mg I, Na I, and Ca II absorption lines in the Gemini spectrum.

3. *J1314−4912*. $z = 2.295$ quasar + star. Source 1 shows broad C IV, C III] and Mg II emission lines at $z = 2.295$, while Source 2 shows Mg I, Na I, and Ca II absorption lines in the Gemini spectra.

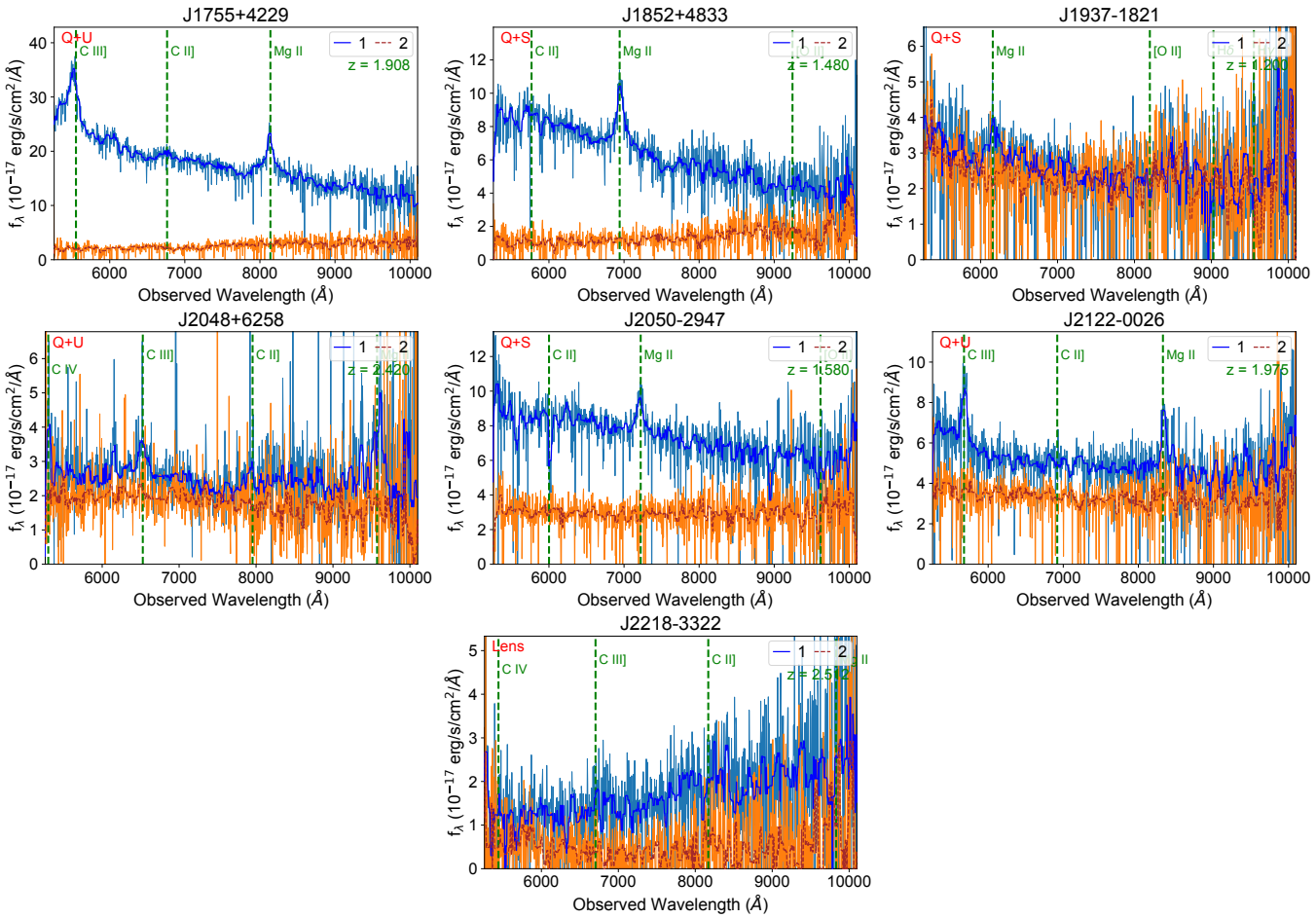

Figure 2. HST STIS optical spectra of 22 targets (seven in this figure and seven in Figure 1). Notations are the same as those in Figure 1.

4. *J1649+0812*. $z = 1.391$ quasar + star. Source 1 shows broad Mg II emission lines at $z = 1.391$ in both the HST and Gemini spectra. Source 2 exhibits H and Ca II absorption lines in the Gemini spectrum. The broad Mg II and narrow [O II] emission lines seen in Source 2 in the Gemini spectra are due to contamination from Source 1. High angular resolution Very Large Telescope (VLT)/MUSE spectra (private communication) confirm the presence of the same absorption features in Source 2, without any accompanying emission lines.
5. *J1711-1611*. $z = 0.790$ quasar + star. Source 1 shows broad H and Hγ emission lines in the HST spectrum, and broad Mg II emission lines in the Gemini spectrum at $z = 0.790$. Source 2 shows Mg I, Na I, and H absorption lines in the Gemini spectrum.
6. *J1732−1335*. $z = 0.292$ quasar + star. Source 1 shows broad H , H , and Hγ emission lines at $z = 0.292$, and Source 2 shows H absorption lines in the Gemini spectra. The emission lines (e.g., H and H) seen in Source 2 are due to contamination from Source 1.
7. *J1804+3230*. $z = 0.504$ quasar + star. Source 1 shows broad H , H , and Hγ emission lines at $z = 0.504$, and Source 2 shows Na I and Ca II absorption lines in the Gemini spectra.
8. *J1852+4833*. $z = 1.480$ quasar + star. Source 1 shows broad Mg II emission lines at $z = 1.480$ in both HST and Gemini spectra. Source 2 shows Na I and Ca II absorption lines in the Gemini spectrum.
9. *J1857+7048*. $z = 1.230$ quasar + star. Source 1 shows broad Mg II emission lines at $z = 1.230$, and Source 2 shows broad, strong Ca II and TiO absorption lines in the Gemini spectra.
10. *J1937-1821*. $z = 1.200$ quasar + star. Source 1 shows broad Mg II emission lines at $z = 1.200$ in both HST and Gemini spectra. Source 2 shows a H absorption line in the Gemini spectrum.
11. *J2050-2947*. $z = 1.580$ quasar + star. Source 1 shows broad Mg II emission lines at $z = 1.580$ in both HST and Gemini spectra. Source 2 shows Mg I and Na I absorption lines in the Gemini spectrum.

3.2.2. Dual/Lensed Quasars

For the following targets, we detect broad emission lines in both sources. Distinguishing between dual quasars and lensed quasars is challenging because the spectra of both sources in most of our dual/lensed quasar candidates are very similar. For example, J0749+2255 and J0823+2418 were confirmed as a dual quasar and a lensed quasar, respectively, based on additional multiwavelength observations (Y.-C. Chen et al. 2023b; A. C. Gross et al. 2023). However, in the absence of definitive evidence from other observations or the literature, we do not distinguish between dual and lensed quasars in this paper. The classifications are listed below.

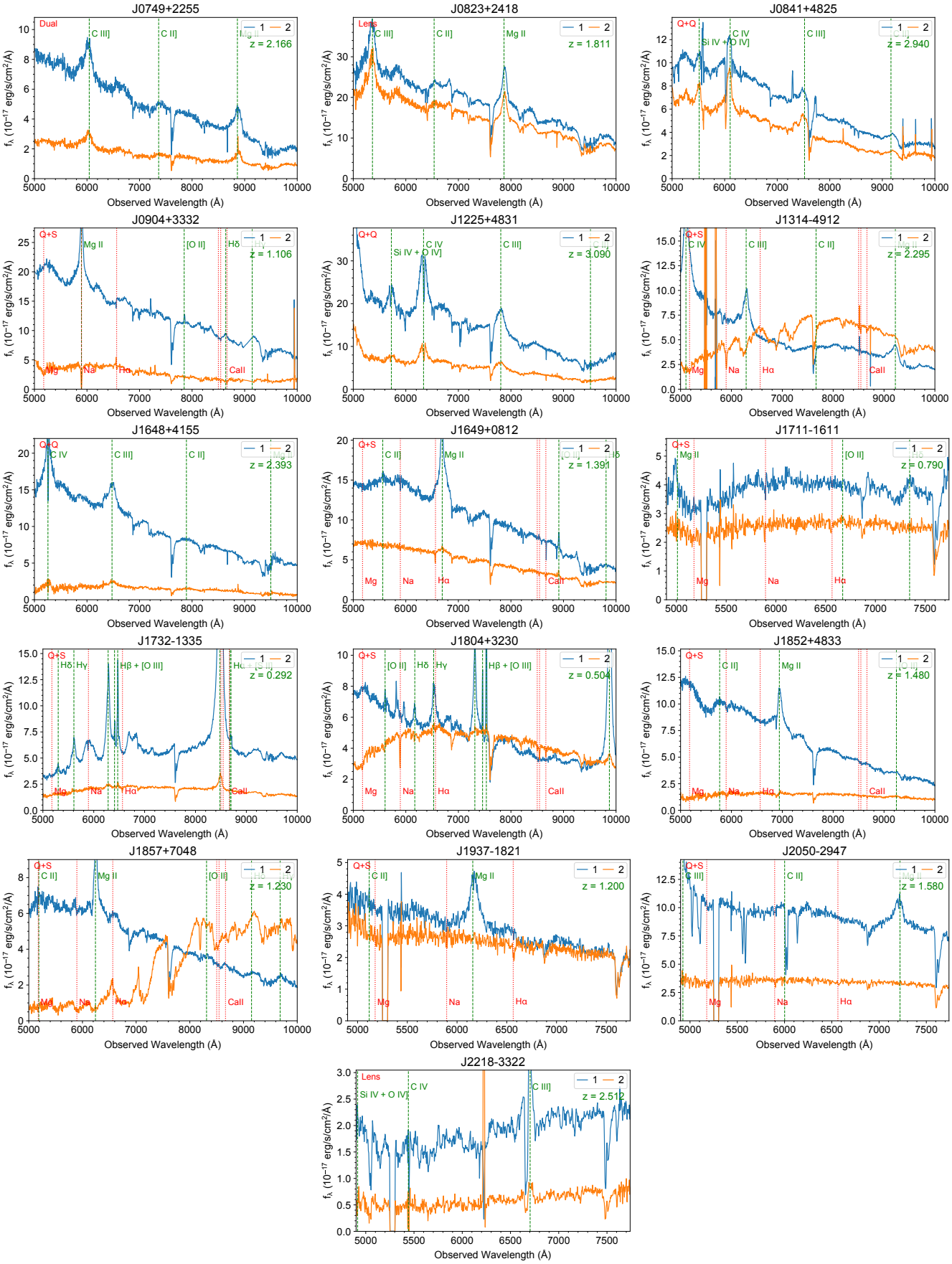

Figure 3. Gemini GMOS optical spectra of 16 targets. Spatially resolved spectra for both sources are shown in solid blue and dashed orange lines. Green vertical dashed lines mark the quasar's emission lines at the systemic redshift, displayed in the top-right corner. Red vertical dotted lines indicate stellar absorption features for star-superposition. Final classifications based on both Gemini and/or HST spectra are shown in the top-left corner (Q: quasar, S: star, U: unknown, Dual: dual quasar, Lens: lensed quasar).

Table 2
Properties and Classifications of the 27 Targets

Abbreviated Name (J2000) (1)	R.A. (deg) (2)	Decl. (deg) (3)	Sep. ( ) (4)	Target Cat. (5)	Color Selection (6)	Spectroscopic Classification (7)
WISE J0241+7801	40.395481	78.018624	0.58	2	Quasar+star	Likely quasar+quasar
WISE J0246+6922	41.619305	69.376122	0.49	5	Quasar+star	**Binary star**
WISE J0348−4015	57.119449	−40.253662	0.50	3	Dual/lensed quasar	**Dual/lensed quasar($z = 2.633$)**
WISE J0536+5038	84.084298	50.6406250	0.32	2	Dual/lensed quasar	Quasar($z = 1.855$) + unknown
SDSS J0748+3146	117.002307	31.779856	0.53	4	Dual/lensed quasar	Quasar($z = 1.407$) + unknown
SDSS J0749+2255	117.345694	22.919936	0.46	1	Dual/lensed quasar	**Dual quasar($z = 2.166$)**
SDSS J0753+4247	118.460738	42.795529	0.33	1	Quasar+star	Quasar($z = 1.523$) + unknown
SDSS J0823+2418	125.921169	24.301570	0.64	4	Dual/lensed quasar	**Lensed quasar($z = 1.811$)**
SDSS J0841+4825	130.374046	48.430135	0.46	1	Dual/lensed quasar	**Dual/lensed quasar($z = 2.940$)**
SDSS J0904+3332	136.036118	33.534796	0.30	1	Quasar+star	**Quasar($z = 1.106$) + star**
SDSS J1225+4831	186.327776	48.521147	0.90	4[a]	…[a]	**Dual/lensed quasar($z = 3.090$)**
WISE J1314−4912	198.566742	−49.205070	0.52	6	Quasar+stars	**Quasar($z = 2.295$) + star**
SDSS J1327+1036	201.966887	10.607564	0.75	1[a]	…[a]	Quasar($z = 1.904$)+ likely quasar
WISE J1613−2644	243.456316	−26.742377	0.28	2	Quasar+star	Unknown
SDSS J1648+4155	252.075328	41.930608	0.44	1	Dual/lensed quasar	**Dual/lensed quasar($z = 2.393$)**
WISE J1649+0812	252.422063	8.209311	0.59	5	Dual/lensed quasar	**Quasar($z = 1.391$) + star**
WISE J1711−1611	257.916584	−16.196649	0.67	5	Dual/lensed quasar	**Quasar($z = 0.790$) + star**
WISE J1732−1335	263.095334	−13.593137	0.72	2	Dual/lensed Quasar+star	**Quasar($z = 0.292$) + star**
WISE J1755+4229	268.929920	42.490069	0.59	5	Quasar+star	Quasar($z = 1.908$) + unknown
WISE J1804+3230	271.039815	32.508215	0.68	5	Quasar+star	**Quasar($z = 0.504$) + star**
WISE J1852+4833	283.108771	48.554173	0.62	2	Quasar+star	**Quasar($z = 1.480$) + star**
WISE J1857+7048	284.369408	70.803154	0.61	5	Quasar+star	**Quasar($z = 1.230$) + star**
WISE J1937−1821	294.328398	−18.358950	0.62	2	Dual/lensed quasar	**Quasar($z = 1.200$) + star**
WISE J2048+6258	312.200003	62.98286	0.62	5	Dual/lensed quasar	Quasar($z = 2.420$) + unknown
WISE J2050−2947	312.500061	−29.789362	0.65	5	Dual/lensed quasar	**Quasar($z = 1.580$) + star**
SDSS J2122−0026	320.679218	−0.448282	0.52	4	Dual/lensed quasar	Quasar($z = 1.975$) + unknown
WISE J2218−3322	334.707755	−33.378782	0.49	5	Quad lens	**Quad lens($z = 2.512$)**

Notes. Column (1): Target name. Column (2): R.A.. Column (3): decl.. Column (4): Pair separation in arcsecond. Column (5): Target category from Y.-C. Chen et al. (2022) (1: SDSS Gaia-unresolved, 2: WISE+PS1 Gaia-unresolved, 3: WISE-only Gaia-unresolved, 4: SDSS Gaia-resolved, 5: WISE+PS1 Gaia-resolved, 6: WISE-only Gaia-resolved). Column (6): Photometric classification using HST F475W and F814W images from Y.-C. Chen et al. (2022). Column (8): Spectroscopic classification based on the optical spectra in this paper. Entries in boldface indicate confirmed classifications.
[a] J1225+4831 and J1327+1036 were not observed in the HST snapshot imaging program (Y.-C. Chen et al. 2022), but they were discovered using the same VODKA technique.

1. *J0348−4015*. Dual/lensed quasar at $z = 2.633$. Both sources show broad C IV emission lines at $z = 2.633$ in the HST spectra. The low signal-to-noise ratio in the HST spectra prevents us from conducting further analysis.
2. *J0749+2255*. Dual quasar at $z = 2.166$. Both sources show broad C III] and Mg II emission lines at $z = 2.166$ in the Gemini spectra. Y.-C. Chen et al. (2023b) detected the host galaxy and tidal tails through multiwavelength observations, confirming the system as a dual quasar.
3. *J0823+2418*. Lensed quasar at $z = 1.811$. Both sources display broad C III] and Mg II emission lines at $z = 1.811$ in both the Gemini and HST spectra. A. C. Gross et al. (2023) identified the lensing galaxy in the HST near-infrared image, and the relative positions of the components are consistent with the lensing model.
4. *J0841+4825*. Dual/lensed quasar at $z = 2.940$. Both sources exhibit broad C III] and C IV emission lines at $z = 2.940$ in both the Gemini and HST spectra. F. Mannucci et al. (2022) classified the system as a dual quasar based on the presence of weak C III]1909 and N III]1750 lines detected only in the secondary source in the HST spectrum. However, we do not observe these features in the higher signal-to-noise Gemini spectrum. Given that the two sources display very similar spectral features in the Gemini data, we consider both the dual and lensed quasar scenarios to be plausible.
5. *J1225+4831*. Dual/lensed quasar at $z = 3.090$. Both sources exhibit broad C III] and C IV emission lines at $z = 3.090$ in the Gemini spectra.
6. *J1648+4155*. Dual/lensed quasar at $z = 2.393$. Both sources exhibit broad H emission lines at $z = 2.393$ in both the Gemini and HST spectra. The broad H emission in Source 2 is unlikely due to spectral contamination from Source 1 because it is also present in the HST spectrum.
7. *J2218−3322*. Quadruply lensed broad absorption line (BAL) quasar at $z = 2.550$. HST optical imaging reveals four background quasar images arranged around a foreground lens galaxy (Y.-C. Chen et al. 2022). Our Gemini spectra confirm the background quasar's redshift at $z = 2.550$ with the C IV emission line and show that it is a BAL quasar.

Figure 4 shows the median-normalized spectra of the seven dual/lensed quasars, highlighting the similarities and differences between the two spectra for each system.

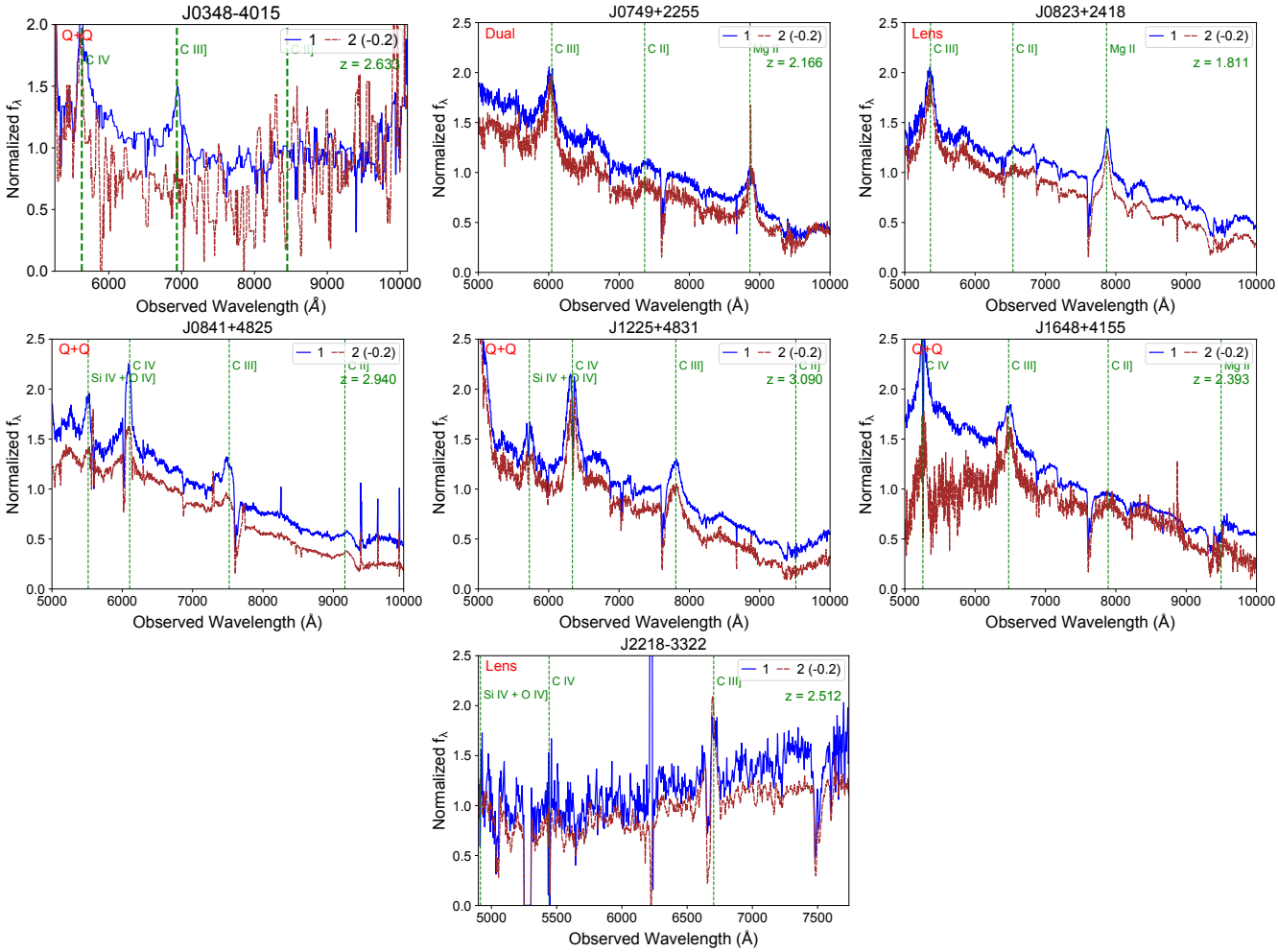

Figure 4. Median-normalized spectra of the seven dual/lensed quasars, with the second source spectra shifted by −0.2 to prevent overlap. Spatially resolved spectra for both sources are represented by solid blue and dashed brown lines. Quasar emission lines at the corresponding redshift (indicated in the top-right corner) are marked by green vertical lines.

3.2.3. Unknown Cases

For the nine remaining targets, we either detect only one broad emission line or are unable to identify any emission or absorption lines. Most of the sources only have low signal-to-noise HST spectra, which prevent us from identifying any absorption lines. We also examine radio observations for some targets (A. C. Gross et al. 2024, in preparation) to identify potential obscured quasars.

1. *J0241+7801*. Both sources are likely quasars with unknown redshifts. Source 1 shows a possible emission line at 8500 Å in the HST spectrum, while Source 2 has a radio detection of >2 mJy (A. C. Gross et al. 2024, in preparation).
2. *J0536+5038*. $z = 1.855$ quasar + unknown source. Source 1 shows broad Mg II and C III] emission lines at $z = 1.855$, while Source 2 shows a featureless flat spectrum in the HST spectra.
3. *J0748+3146*. $z = 1.407$ quasar + unknown source. Source 1 exhibits broad Mg II emission lines at $z = 1.407$, while Source 2 shows no significant spectral features in the HST spectra.
4. *J0753+4247*. $z = 1.523$ quasar + unknown source. Source 1 exhibits broad Mg II and C II] emission lines at $z = 1.523$, while Source 2 shows no significant spectral features in the HST spectra.
5. *J1327+1036*. $z = 1.904$ quasar + a likely quasar. Source 1 exhibits broad Mg II and C III] emission lines at $z = 1.904$, while Source 2 shows no significant spectral features in the HST spectra. Both sources are detected in the radio at the mJy level, likely indicating quasar activity (A. C. Gross et al. 2024, in preparation).
6. *J1613-2644*. Unknown case. No emission lines are detected in both sources in the HST spectra.
7. *J1755+4229*. $z = 1.908$ quasar + unknown source. Source 1 exhibits broad Mg II and C III] emission lines at $z = 1.908$, while Source 2 shows no significant spectral features in the HST spectra.
8. *J2048+6258*. $z = 2.420$ quasar + unknown source. Source 1 exhibits broad Mg II, C II] and C III] emission lines at $z = 2.420$, while Source 2 shows no significant spectral features in the HST spectra.
9. *J2212-0026*. $z = 1.975$ quasar + unknown source. Source 1 exhibits broad Mg II and C III] emission lines at

Table 3
Fraction of Quasar-star Superpositions and Dual/Lensed Quasars

Sample (1)	# (2)	Dual/Lens (3)	Quasar-star (4)
1. Whole follow-up sample	25	$\gtrsim$26%	41%–67%
2. SDSS quasars only	10	$\gtrsim$50%	10%–40%
3. F475W−F814W color cut	15	$\gtrsim$40%	33%–60%
4. Criteria 2 and 3	6	$\gtrsim$67%	0%–33%

Note. Column (1): Sample selection. Column (2): Number of targets. Column (3): Dual/lensed quasar fraction 4: Quasar-star-superposition fraction. F475W −F814W color cut is mainly based on the photometric classification in Y.-C. Chen et al. (2022).

$z = 1.975$, while Source 2 shows no significant spectral features in the HST spectra.

4. Discussion

4.1. Quasar-star-superposition and Dual/Lensed Quasar Fractions

Based on the two-band color cut using HST F475W and F814W images, Y.-C. Chen et al. (2022) estimated a quasar-star-superposition rate of 30% 10% for the targets in the VODKA project. However, this simple two-band color cut method primarily differentiates late-type stars from typical unobscured quasars, potentially misclassifying early-type stars and obscured quasars. With our spectroscopic follow-up observations, we can now provide a more accurate assessment of the fractions of star superpositions and dual/lensed quasars.

Among the 45 targets discovered in the VODKA imaging project (Y.-C. Chen et al. 2022) and additional targets from various subsequent campaigns, we observed 25 with our spectroscopic data. For these observed targets, we calculated a star-superposition rate of $11/27 = 41\%$. This is likely a lower limit because we selectively followed up on targets with blue and similar colors, and additional quasar-star superpositions may be present among the uncertain cases. Assuming that targets with unknown companions are all quasar-star superpositions, the upper limit of the quasar-star-superposition rate is $18/27 = 67\%$. This 41%–67% superposition rate exceeds the estimated rate of 30% 10% from the two-band color cut (Y.-C. Chen et al. 2022). The higher rate is likely due to the exclusion of stars (e.g., F and G stars) with similar optical colors to quasars in the two-band color cut. For dual/lensed quasars, counting only those confirmed spectroscopically from spatially resolved spectra, we obtained a fraction of $7/27 = 26\%$. This fraction is a lower limit, as additional dual/lensed quasars might not have been discovered due to low signal-to-noise spectra or because they were not observed due to redder colors.

We can evaluate whether additional selection criteria could yield a cleaner sample. For instance, if we restrict our candidates to those identified as spectroscopically confirmed quasars and apply the same reasoning as before, we find that the quasar-star-superposition rate ranges from $1/10 = 10\%$ to $4/10 = 40\%$. Additionally, the lower limit for the fraction of dual/lensed quasars increases to $5/10 = 50\%$.

We can examine whether extra selection criteria can provide a cleaner sample. For example, if we only select candidates from spectroscopically confirmed quasars and following the same argument in the previous paragraph, we can obtain the quasar-star-superposition rate between $1/10 = 10\%$ and $4/10 = 40\%$, and the lower limit of dual/lensed quasar fraction is $5/10 = 50\%$. Similar calculations can be performed by considering only the targets classified as dual/lensed quasar candidates using HST F475W and F814W images (Y.-C. Chen et al. 2022). The quasar-star-superposition and dual/lensed quasar fractions for various samples are listed in Table 3. In summary, with existing unresolved spectra from the Sloan Digital Sky Survey (SDSS) and the spatially resolved two-band color cut, the fraction of dual/lensed quasars can be pushed to higher than 67%.

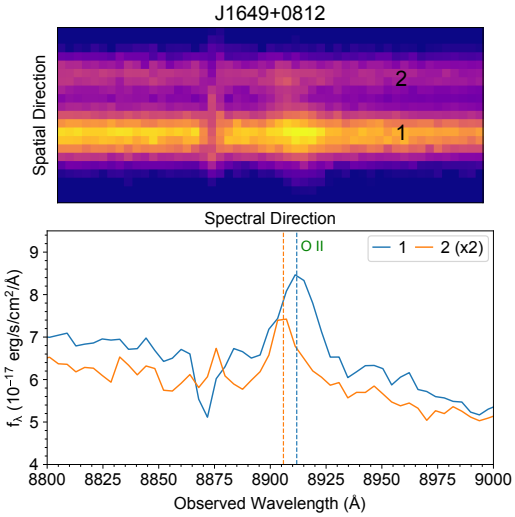

Figure 5. Top: marginally resolved 2D spectrum of J1649+0812, showing the traces of two sources and the [O II] emission. Bottom: Extracted 1D spectra of J1649+0812, showing a possible velocity offset of 200 km s^{-1} between the [O II] emission lines. However, given that Source 2 is a star, this velocity offset is likely due to internal orbital motion within a single host galaxy. The [O II] emission line observed in Source 2 likely originates from the extended host galaxy of Source 1, rather than from Source 2 itself.

4.2. J1649+0812: A Cautionary Tale of Sources with Velocity Offsets

J1649+0812 was initially classified as a dual quasar when we submitted the draft, based on the detection of a broad Mg II emission line in Source 2 and a possible velocity offset of 183 76 km s^{-1} between the two sources in the narrow [O II] emission line (Figure 5). However, further analysis of the Gemini spectrum reveals that Source 2 is a star, as indicated by the presence of H and Ca II absorption lines. The adaptive optics-assisted VLT/MUSE data with higher angular resolution (FWHM 0.″1) and improved signal-to-noise ratio (private communication) also show that the weak broad Mg II feature is likely an artifact of the marginally resolved Gemini spectra (FWHM 0.″5), and is not detected in the resolved HST spectrum (FWHM 0.″1). The 200 km s^{-1} velocity offset in [O II] likely arises from internal orbital motion within a single host galaxy. The [O II] emission line observed in Source 2 likely originates from the extended host galaxy of Source 1, rather than from Source 2 itself. We caution that small velocity offsets ($\lesssim$300 km s^{-1}) in narrow emission lines should not be used as standalone evidence for identifying dual quasars, particularly in marginally resolved spectra.

4.3. Implication for Future Spectroscopic Follow-ups

Based on the results of this study, we outline the following implications for future spectroscopic follow-up to confirm the nature of dual quasar candidates:

1. Given the high star-superposition rate (37%–63%), we suggest performing detailed spectral decomposition for targets with existing spectra (e.g., SDSS) before conducting follow-up observations. Y. Shen et al. (2023) successfully used spectral principal component analysis to identify potential star superpositions, revealing star companions of various types. Applying similar spectral decomposition to existing spectra can help reduce the star-superposition rate and better allocate limited telescope time to higher-confidence dual/lensed quasar candidates.
2. A decent signal-to-noise ratio for the continuum is essential to detect absorption lines such as Na I, H , and Mg I, particularly for F- and G-type stars. We recommend a signal-to-noise ratio of $\gtrsim$20 per spectral element. In our data, the Gemini spectra achieve a signal-to-noise ratio of at least 20 per spectral element, whereas the HST/STIS spectra range from 1 to 10 per spectral element.
3. High spatial resolution is essential to avoid spectral contamination from the primary source to the secondary source. Some of our targets suffer from blending in the Gemini spectra, which have angular resolutions comparable to the separations between sources. We recommend using spatial resolution at least twice as high (i.e., FWHM no more than half the source separation) to reliably disentangle the spectra of close pairs.
4. High spectral resolution may be necessary to reliably identify velocity offsets in dual quasars. However, small velocity offsets should not be used as standalone evidence for dual quasar identification, especially in marginally resolved spectra. We recommend a spectral resolution of $R \gtrsim 1000$ (corresponding to 300 km s^{-1}), which is sufficient to resolve offsets larger than typical galaxy rotation velocities.

5. Conclusion

In this paper, we present extensive spectroscopic follow-up observations of 27 dual quasar candidates identified by the VODKA project. Using data from Gemini/GMOS and HST/STIS, we classify and assess the nature of these systems. We identify 11 cases as star-quasar superpositions and seven systems as either dual or lensed quasars. For the remaining nine targets, a conclusive classification is not possible, although two are likely dual quasars based on supporting radio data. Among the seven dual/lensed quasars, three had been previously confirmed in the literature. Additionally, we determine the redshift of the background quasar in a quadruply lensed system, for which the redshift was previously unknown.

Our follow-up observations yield a star-superposition rate of 41%–67% in the VODKA sample, which exceeds previous estimates. The fraction of dual/lensed quasars is at least 30%. The higher quasar-star-superposition rate is likely due to the lack of initial color selection or spectral decomposition for the initial VODKA sample. By leveraging unresolved SDSS spectra and spatially resolved two-band color cuts, we estimate that the dual/lensed quasar fraction could exceed 67%. The ongoing HST snapshot program (Program ID: SNAP-17455; PI: Shen) incorporates various selection criteria to obtain a cleaner sample of dual/lensed quasar candidates. Further multiwavelength observations and detailed analysis of narrow emission lines are necessary to better differentiate between dual and lensed quasars. Our study highlights the critical need for high-quality spectral data—with a signal-to-noise ratio of $\gtrsim$20, spatial resolution at least twice finer than the source separation, and spectral resolution of $R \gtrsim 1000$—to effectively separate close sources, rule out stellar superpositions, and reliably identify dual quasars.

Acknowledgments

We thank the anonymous referee for giving constructive comments. We thank Michael Leveille, Alison Vick, Kristin Chiboucas, Hwihyun Kim, Trent Dupuy, Atsuko Nitta, Siyi Xu, and Rodolfo Angeloni for their help with our HST and Gemini observations. We thank Dr. Filippo Mannucci for his valuable and constructive comments. This work is supported by NSF grant AST-2108162. Y.S. acknowledges partial support from NSF grant AST-2009947. Support for Program number HST-GO-16210 and HST-GO-16887 (PI: X.L.) was provided by NASA through grants from the Space Telescope Science Institute, which is operated by the Association of Universities for Research in Astronomy, Incorporated, under NASA contract NAS 5-26555. Based on observations made with the NASA/ESA Hubble Space Telescope, obtained from the Data Archive at the Space Telescope Science Institute, which is operated by the Association of Universities for Research in Astronomy, Inc., under NASA contract NAS 5-26555. These observations are associated with programs GO-16210 and GO-16887.

Based in part on observations obtained at the international Gemini Observatory (Program IDs GN-2020A-DD-106, GN-2022A-Q-139, and GS-2022A-Q-148; PI: X. Liu, and GN-2020A-Q-232; PI: Y.-C.C.), a program of NSF's NOIRLab, which is managed by the Association of Universities for Research in Astronomy (AURA) under a cooperative agreement with the National Science Foundation on behalf of the Gemini Observatory partnership: the National Science Foundation (United States), National Research Council (Canada), Agencia Nacional de Investigación y Desarrollo (Chile), Ministerio de Ciencia, Tecnologìa e Innovación (Argentina), Ministério da Ciência, Tecnologia, Inovações e Comunicações (Brazil), and Korea Astronomy and Space Science Institute (Republic of Korea). This work was enabled by observations made from the Gemini-North telescope, located within the Maunakea Science Reserve and adjacent to the summit of Maunakea. We are grateful for the privilege of observing the Universe from a place that is unique in both its astronomical quality and its cultural significance.

Facilities: HST (STIS), Gemini:Gillett, Gemini:South.

Software: NumPy (C. R. Harris et al. 2020), astropy (Astropy Collaboration et al. 2013, 2018, 2022)

ORCID iDs

Yu-Ching Chen https://orcid.org/0000-0002-9932-1298
Arran C. Gross https://orcid.org/0000-0001-7681-9213
Xin Liu https://orcid.org/0000-0003-0049-5210
Yue Shen https://orcid.org/0000-0003-1659-7035
Nadia L. Zakamska https://orcid.org/0000-0001-6100-6869

Hsiang-Chih Hwang https://orcid.org/0000-0003-4250-4437
Ming-Yang Zhuang https://orcid.org/0000-0001-5105-2837

References

Anderson, J., & Bedin, L. R. 2010, PASP, 122, 1035
Astropy Collaboration, Price-Whelan, A. M., Lim, P. L., et al. 2022, ApJ, 935, 167
Astropy Collaboration, Price-Whelan, A. M., Sipőz, B. M., et al. 2018, AJ, 156, 123
Astropy Collaboration, Robitaille, T. P., Tollerud, E. J., et al. 2013, A&A, 558, A33
Barnes, J. E. 2002, MNRAS, 333, 481
Barnes, J. E., & Hernquist, L. 1996, ApJ, 471, 115
Breiding, P., Chiaberge, M., Lambrides, E., et al. 2024, ApJ, 963, 91
Capelo, P. R., & Dotti, M. 2017, MNRAS, 465, 2643
Chen, N., Di Matteo, T., Ni, Y., et al. 2023a, MNRAS, 522, 1895
Chen, Y.-C., Hwang, H.-C., Shen, Y., et al. 2022, ApJ, 925, 162
Chen, Y.-C., Liu, X., Foord, A., et al. 2023b, Natur, 616, 45
Ciurlo, A., Mannucci, F., Yeh, S., et al. 2023, A&A, 671, L4
Cole, S., Lacey, C. G., Baugh, C. M., & Frenk, C. S. 2000, MNRAS, 319, 168
De Rosa, A., Vignali, C., Bogdanović, T., et al. 2019, NewAR, 86, 101525
Ellison, S. L., Viswanathan, A., Patton, D. R., et al. 2019, MNRAS, 487, 2491
Fan, L., Han, Y., Fang, G., et al. 2016, ApJL, 822, L32
Gross, A. C., Chen, Y.-C., Foord, A., et al. 2023, ApJ, 956, 117
Harris, C. R., Millman, K. J., van der Walt, S. J., et al. 2020, Natur, 585, 357
Hernquist, L. 1989, Natur, 340, 687
Hopkins, P. F., & Quataert, E. 2010, MNRAS, 407, 1529
Hwang, H.-C., Shen, Y., Zakamska, N., & Liu, X. 2020, ApJ, 888, 73
Kormendy, J., & Ho, L. C. 2013, ARA&A, 51, 511
Lemon, C., Anguita, T., Auger-Williams, M. W., et al. 2023, MNRAS, 520, 3305
Lemon, C. A., Auger, M. W., & McMahon, R. G. 2019, MNRAS, 483, 4242
Lemon, C. A., Auger, M. W., McMahon, R. G., & Ostrovski, F. 2018, MNRAS, 479, 5060
Magorrian, J., Tremaine, S., Richstone, D., et al. 1998, AJ, 115, 2285
Mannucci, F., Pancino, E., Belfiore, F., et al. 2022, NatAs, 6, 1185
Mannucci, F., Scialpi, M., Ciurlo, A., et al. 2023, A&A, 680, A53
Mechtley, M., Jahnke, K., Windhorst, R. A., et al. 2016, ApJ, 830, 156
Mihos, J. C., & Hernquist, L. 1996, ApJ, 464, 641
Navarro, J. F., Frenk, C. S., & White, S. D. M. 1996, ApJ, 462, 563
Rosas-Guevara, Y. M., Bower, R. G., McAlpine, S., Bonoli, S., & Tissera, P. B. 2019, MNRAS, 483, 2712
Scialpi, M., Mannucci, F., Marconcini, C., et al. 2024, A&A, 690, A57
Shen, Y., Hwang, H.-C., Oguri, M., et al. 2023, ApJ, 943, 38
Shen, Y., Hwang, H.-C., Zakamska, N., & Liu, X. 2019, ApJL, 885, L4
Steinborn, L. K., Dolag, K., Comerford, J. M., et al. 2016, MNRAS, 458, 1013
Volonteri, M., Pfister, H., Beckmann, R., et al. 2022, MNRAS, 514, 640
White, S. D. M., & Frenk, C. S. 1991, ApJ, 379, 52